Baghdad Science Journal

Volume 23 | Issue 4 Article 8

4-20-2026

Infinitely Many Hidden Attractors in a Simple Six-Term Chaotic 2-torus Snap System with a Line of Equilibria

Sarbast Hussein Mikaeel
Department of Mathematics, Faculty of Science, Soran University, Soran, Kurdistan Region, Iraq,
sarbast.mikael@soran.edu.iq

Irfan Ahmad
School of Computing and Mathematical Sciences, The University of Waikato, New Zealand,
Irfan.Ahmad@waikato.ac.nz

Rizgar H. Salih
Department of Mathematics, College of Basic Education, University of Raparin, Rania, Kurdistan Region, Iraq, rizgar.salih@uor.edu.krd

How to Cite this Article

Mikaeel, Sarbast Hussein; Ahmad, Irfan; and Salih, Rizgar H. (2026) "Infinitely Many Hidden Attractors in a Simple Six-Term Chaotic 2-torus Snap System with a Line of Equilibria," *Baghdad Science Journal*: Vol. 23: Iss. 4, Article 8.
DOI: https://doi.org/10.21123/2411-7986.5262

BAGHDAD SCIENCE JOURNAL 2026;23(4):1220–1240

Scan the QR to view the full-text article on the journal website

RESEARCH ARTICLE

Infinitely Many Hidden Attractors in a Simple Six-Term Chaotic 2-torus Snap System with a Line of Equilibria

Sarbast Hussein Mikaeel [1,*], **Irfan Ahmad** [2], **Rizgar H. Salih** [3]

[1] Department of Mathematics, Faculty of Science, Soran University, Soran, Kurdistan Region, Iraq
[2] School of Computing and Mathematical Sciences, The University of Waikato, New Zealand
[3] Department of Mathematics, College of Basic Education, University of Raparin, Rania, Kurdistan Region, Iraq

ABSTRACT

Chaotic systems with simple structures and controllable dynamics are highly desirable for practical applications, including secure communications, signal processing, and nonlinear control. However, most existing systems are too complex or lack flexibility in controlling signal amplitude and polarity. In this study, a simple chaotic snap system is considered that has a line of equilibria and is composed of six algebraic terms, with a single quadratic nonlinearity. In some regions of parameter space, a chaotic attractor coexists with a line equilibrium or with a limit cycle of period-2. The basin boundary of a limit cycle and chaotic attractor is smooth. Additionally, in specific regions, two limit cycles can coexist each other. A single quadratic term allows rescaling chaotic signal amplitude, while adding a constant to x controls polarity. The snap system can become self-reproducing via periodic functions, producing a 3D lattice of hidden attractors with identical Lyapunov exponents. Consequently, a chaotic signal of either polarity can be obtained by selecting different initial conditions without requiring an additional polarity converter. These properties allow the implementation of a digital circuit based on STM32 hardware to illustrate the physical feasibility of the proposed system. Finally, to validate the feasibility of the snap system for image encryption a random number generator (RNG) is implemented. The generated RNG successfully passes the National Institute of Standards and Technology (NIST) SP 800-22 statistical tests. Based on these random bits, an image encryption algorithm is developed. Security analysis confirms the system effectively encrypts and decrypts images with high performance.

Keywords: Amplitude and polarity control, Hardware implementation, Hidden attractors, Image encryption, Multistability, Self-reproducing system, Snap system

Introduction

The exploration of chaotic dynamics in nonlinear systems has been at the forefront of the field since Edward Lorenz's pioneering research in 1963.[1] This area has seen exceptional development because it is extensively applied to different scientific areas and engineering domains, especially in secure communication systems using chaos-based encryption models.[2–4]

Traditionally, three-dimensional (3D) autonomous chaotic systems are mathematically described through coupled first-order ordinary differential equations (ODEs) involving three state variables, conventionally denoted as $(x,\ y,\ z)$. A paradigmatic example of such systems is Chua's circuit, which has served as a cornerstone for understanding circuit-based chaos.[5] Alternatively, chaotic behavior can be elegantly captured through a single third-order ODE of the form $\dddot{x} = J(x, \dot{x}, \ddot{x})$, commonly designated

Received 8 April 2025; revised 4 November 2025; accepted 18 November 2025.
Available online 20 April 2026

* Corresponding author.
E-mail addresses: sarbast.mikael@soran.edu.iq (S. H. Mikaeel), Irfan.Ahmad@waikato.ac.nz (I. Ahmad), rizgar.salih@uor.edu.krd (R. H. Salih).

https://doi.org/10.21123/2411-7986.5262

as a jerk system.[6–9] These jerk systems have garnered substantial attention in nonlinear dynamics research due to their remarkable combination of structural simplicity and complex dynamical behaviors.[10–12]

From a physical perspective, in Newtonian mechanics, the derivatives $\frac{dx}{dt}$, $\frac{d^2x}{dt^2}$ and $\frac{d^2x}{dt^2}$ represent displacement, velocity and acceleration, respectively. When a jerk system's dynamics are governed by a fourth-order derivative of the form $\frac{d^4x}{dt^4} = J(x, \frac{d^3x}{dt^3}, \frac{d^2x}{dt^2}, \frac{dx}{dt})$, it is classified as a hyperjerk system or snap system.[13] The fourth derivative $\frac{d^4x}{dt^4}$ is commonly referred to as "snap" in the literature, though alternative terms such as "jounce," "sprite," or "surge" are occasionally employed.[13] Fourth-order (4D) hyperjerk ODEs can describe either 4D chaotic hyperjerk systems[14–16] or 4D hyperchaotic hyperjerk systems.[17]

Hyperjerk systems have substantial physical importance due to their capacity to describe motions whose acceleration dynamics are even more complex, which leads to a more sophisticated and realistic representation of motion. Use of higher-order derivatives, especially snap, helps their models capture real-world dynamics featuring many interacting variables and high-dimensional phase spaces of common occurrence within mechanical, electrical and biological systems.[18,19] This more advanced mathematical framework can help study complex dynamics, from hyperchaos and multi-scroll attractors to complex transient dynamics with an emphasis on enhancing hyperjerk systems as fundamental resources for modeling and control of advanced dynamical systems.[20–22]

In a systematic introduction to the generalized Chua's system, the first hidden attractor was discovered in 2010.[23,24] This established a foundational classification of attractors, which includes self-excited and hidden attractors. A self-excited attractor has a basin of attraction that intersects with the neighborhood of an equilibrium point, as shown by classical Lorenz system attractors.[1] In contrast, a hidden attractor has a basin of attraction that does not overlap with any neighborhood of equilibrium points. Hidden attractors have emerged as an important subject of study to study the unpredictable and catastrophic behavior of dynamical systems in relation to perturbations. Therefore it comes with significant implication in different fields, such as aircraft control, to name a few, where hidden attractors can produce unexpected oscillations which may hamper flight stability systems, drilling operations where they would be exploited because they induce complicated dynamic forces that can affect operational and safety conditions as well as convective fluid flow systems, where they can generate flow profiles with major implications for engineering as well as natural processes.[25–27]

Multistability (also called the coexistence of several stable states in one dynamical system) has been regarded as a universal property across many scientific fields. This behavior is observed in different physical systems, such as laser dynamics[28,29] and optical systems.[30] Multistability is important because it allows flexible system behavior through state transitions controlled by initial conditions, without having to adjust parameters.[31] Multistability protects chaos-based communication as well by allowing additional freedom through initial condition selection, hence generating additional secret keys for cryptography applications.[32–34]

Chaos-based applications, especially for secure communication systems, should yield chaotic signals with the exact control of amplitude and polarity features. Recent advances have introduced sophisticated methods for simultaneously controlling both amplitude and polarity of chaotic signals, enabling fine-tuning of signal properties without inducing undesirable bifurcations.[35] These techniques prove particularly advantageous for practical implementations in chaos-based secure communications, as they minimize hardware requirements while facilitating the generation of chaotic signals with desired specifications.[36] While these control methods have been successfully implemented together in 4D chaotic snap systems with a single equilibrium point[37] and separately in systems with no equilibria[38] or infinite equilibria,[18] their combined application in 4D chaotic snap systems featuring six terms and a line of equilibria that generate hidden attractors remains unexplored.

Chaotic snap systems exhibiting line equilibria and infinite equilibrium points constitute a relatively rare class in the existing literature.[39,40] Notably, systems possessing line equilibria are generally categorized as hidden attractor systems.[41] Current research has identified five chaotic snap systems that demonstrate line equilibria for hidden attractors, incorporating one,[18,42] two,[40] or three[43] nonlinear terms. Among these five systems, three exhibit multistability but necessitate seven[18,42] or eight[39,43] algebraic terms. Significantly, none of these systems has incorporated self-reproducing mechanisms for generating infinitely many hidden attractors, raising the fundamental question of whether a chaotic snap system with merely six algebraic terms and a single nonlinearity could achieve multistability and for line equilibria with hidden attractors.

Recent studies have explored methods for generating an infinite number of coexisting chaotic

attractors.[44–46] A self-reproducing system approach can achieve infinitely many coexisting chaotic attractors, with identical Lyapunov exponents (LEs) across all attractors, realized through variations in initial conditions.[31] Careful selection of these initial conditions allows the generation of chaotic signals with a desired polarity without additional hardware, with multistability providing an effective mechanism for polarity control. To the best of our knowledge, no self-reproducing chaotic snap system exhibiting a line of equilibria and supporting infinitely many hidden attractors has been reported in the literature.

A chaotic snap system characterized by six algebraic terms and a single quadratic nonlinearity is investigated in this paper, as presented in[47]. The zero-Hopf bifurcation and the absence of a $\mathcal{C}^1$ first integral near the origin is analyzed by the authors in[47]. The system is reduced to a 3D form using a polynomial first integral, and its dynamics, including local bifurcations, chaotic behavior, and applications in digital circuits, are examined.

The contents of the paper are as follows: Firstly, the proposed system is presented, and several behaviors are investigated, including the types of attractors, dissipative and conservative properties, boundedness, and multistability. After that, the mechanisms for controlling the amplitude and polarity of chaotic signals in the proposed snap system are described. Next, the self-reproducing behavior with infinitely many attractors is introduced for the proposed system. Then, an experimental platform for the STM32-based hardware implementation is presented for the proposed system. The random number generation (RNG) method is validated using the NIST SP 800-22 statistical test suite, and it is confirmed that all required randomness conditions are satisfied by the proposed system. Finally, the image encryption application is presented, followed by the conclusion and discussion.

The proposed system

This section presents the mathematical formulation of a six-term single-nonlinearity chaotic snap system with a line of equilibria. The analysis includes equilibrium points, eigenvalue characteristics, attractor types, dissipation properties, boundedness conditions, and fundamental dynamic behaviors.

Mathematical model

The proposed chaotic snap system[47] is expressed as:

$$\begin{cases} \dot{x} = y, \\ \dot{y} = z, \\ \dot{z} = w, \\ \dot{w} = -az - bw - xy, \end{cases} \tag{1}$$

where a and b represent real parameters, with a as a bifurcation parameter, and b serving as the damping coefficient. While system (1) can be simplified by setting $b = 0$ for a conservative snap system; chaos vanishes whenever $b < 0.4$, as shown in the analysis later. Thus, the system (1) is the minimal dissipative chaotic snap system involving a single quadratic nonlinearity.

In Table 1, this proposed system is compared to existing chaotic snap systems that feature one, two, or infinite equilibria. Comparisons showed four strong advantages of the proposed system: (i) less algebraic complexity with six terms compared to seven or eight of previous systems, (ii) use of a single quadratic nonlinearity as opposed to many nonlinear terms, (iii) a higher LE_1 value indicating improved instability of the system, and (iv) Lyapunov dimension D_L revealing the improved fractal structure in the boundaries of attractor basins. Although six of the other systems mentioned are multistable, they require

Table 1. System (1) and current chaotic snap systems are compared.

	Number of		Type of		Value of		Existence of	Control of
Ref.	Term	Nonlinearity	Nonlinearity	Equilibria	LE_1,	D_L	Multistabiliy	Amplitude/Offset
[13]	07	01	Quadratic	One	0.0780	2.17	No	No
	07	01	Quadratic	One	0.0310	2.068	No	No
[15]	08	01	Mixed	Infinite	0.1214	2.1666	Yes	No
[18]	07	01	Cubic	Infinite	0.0357	2.0666	Yes	No
[39]	08	01	Quadratic	Infinite	0.0730	3.1300	No	No
[40]	08	02	Cubic	Infinite	0.0894	3.0994	No	No
[42]	07	01	Quadratic	Infinite	0.1245	3.1993	Yes	No
[43]	08	03	Mixed	Infinite	0.0578	3.0969	Yes	No
[48]	07	01	Mixed	One	0.1118	2.2083	Yes	No
[49]	08	02	Quadratic	Two	0.0931	2.3043	Yes	No
This paper	06	01	Quadratic	Infinite	0.1301	3.2455	Yes	Yes

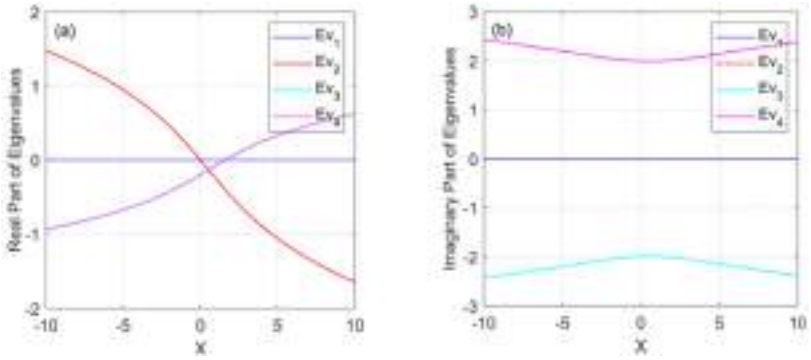

Fig. 1. Eigenvalues of the system (1) along the equilibrium line E, when $a = 4.01$ and $b = 0.4$: (a) Real components; (b) Imaginary components.

additional terms or nonlinearities, while our proposed system (1) achieves equivalent performance by a single quadratic nonlinearity with few terms.

Equilibria and eigenvalues

The equilibrium points of the system (1) are determined by solving $\dot{x} = \dot{y} = \dot{z} = \dot{w} = 0$ simultaneously. The solution yields:

$$E = \left\{ (x^*, y, z, w) \mid y = z = w = 0, \quad x^* \in R \right\}, \tag{2}$$

At equilibrium E, the Jacobian matrix is

$$J_E = \begin{bmatrix} 0 & 1 & 0 & 0 \\ 0 & 0 & 1 & 0 \\ 0 & 0 & 0 & 1 \\ 0 & -x^* & -a & -b \end{bmatrix}, \tag{3}$$

with characteristic equation $|J_E - \lambda I_{4\times 4}| = 0$, yielding:

$$P(\lambda) = \lambda \left(\lambda^3 + b\lambda + a\lambda + x^* \right) = 0. \tag{4}$$

The solution of Eq. (4) for λ produce single zero eigenvalue, while other values depend on a and b. Using the Routh-Hurwitz stability criterion, the three non-zero eigenvalues possess negative real parts when $b > 0$, $x^* > 0$ and $ab - x^* > 0$. Otherwise, the equilibrium line E becomes unstable.

Fig. 1 illustrates the eigenvalue components of the system (1) along the equilibrium line E for $-10 \leq x^* \leq 10$ with $a = 4.01$ and $b = 0.4$. For representative x^*, the eigenvalue characteristics are compiled in Table 2. In general, the cases presented in Table 2 are non-hyperbolic, with $x^* = 0$ and $x^* = 1.6$, specifically identified as critical cases.[50] Due to the existence of at least one eigenvalue with a positive real part for $x^* \in [-10, 0) \in (1.6, 10]$, the local behavior along the equilibrium line becomes unstable.[18,50]

Hidden chaotic attractors

Numerical simulations utilize the fourth-order Runge-Kutta method to ensure both efficiency and reliability in the analysis of dynamical systems. This algorithm demonstrates O(n) computational complexity for fixed time intervals with consistent step sizes, where n denotes the total number of time steps. Implementation utilizes MATLAB's ode45 solver for system (1) integration.

For parameters $a = 4.01$, $b = 0.4$ and initial conditions $(x_0, y_0, z_0, w_0) = (1.3, 1.77, 5.3, 1.08)$, Fig. 2 displays the numerical trajectories of the system (1) across various projection planes. The pink markers indicate the infinite equilibrium line. Since the chaotic attractors exist independently of equilibrium point neighborhoods, the system (1) generates hidden-type chaotic attractors.[47]

Dissipative and conservative properties

Volume contraction characterizes dissipative nonlinear dynamical systems and determines whether

Table 2. Eigenvalues $\lambda_i (i = 1, \ldots, 4)$ at equilibrium set E, when $a = 4.01$ and $b = 0.4$.

x^*	λ_1	λ_2	$\lambda_{3,4}$	Classification
−0.1	0	0.0248	$-0.2124 \pm 1.9938\, i$	Unstable saddle – focus
0	0	0	$-0.2 \pm 1.9924\, i$	Critical case
1.6	0	−0.3990	$-0.0004 \pm 2.0024\, i$	Critical case
2	0	−0.4931	$0.0465 \pm 2.0133\, i$	Unstable saddle – focus

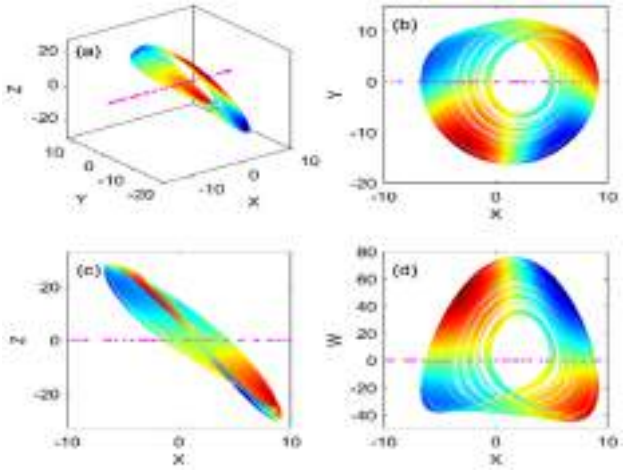

Fig. 2. Phase portraits of the system (1) for a = 4.01, b = 0.4 with initial conditions (1.3, 1.77, 5.3, 1.08).

phase-space volume is conserved. System (1) exhibits dissipative behavior when $b > 0$:

$$\nabla\langle \dot{x}, \dot{y}, \dot{z}, \dot{w}\rangle = \frac{\partial \dot{x}}{\partial x} + \frac{\partial \dot{y}}{\partial y} + \frac{\partial \dot{z}}{\partial z} + \frac{\partial \dot{w}}{\partial w} = -b < 0.$$

The system converges exponentially as e^{-bt}, ensuring orbital volumes approach zero as $t \to \infty$. When $b = 0$, the system becomes conservative. Using the Wolf algorithm with fourth-order Runge-Kutta integration, time step 0.001, simulation duration 1×10^5 units, initial condition (0.1, 0.1, 2, 0) and parameter $a = 4.2$, the computed LEs are $LE_1 = LE_2 = LE_3 = LE_4 = 0$, confirming neutral stability and indicating non-chaotic quasi-periodic behavior.

Boundedness of the system

The boundedness of the chaotic trajectories of the system (1) is demonstrated through the theorem discussed in the literature.[51,52]

Theorem 1: *If the parameters a and b of system (1) If they are positive, then the trajectories of the system, including chaotic orbits, are confined within a bounded region.*

Proof. Assume that $a > 0$ and $b > 0$, consider the Lyapunov function defined as follows: $v(x, y, z, w) = \frac{1}{2}(x^2 + y^2 + z^2 + w^2)$. We take the derivative of v with respect to t, we have

$$\dot{v}(x, y, z, w) = x\dot{x} + y\dot{y} + z\dot{z} + w\,\dot{w}.$$

This equation yields

$$\dot{v}(x, y, z, w) = \left(x + \frac{1}{2}y\right)^2 + \left(y + \frac{1}{2}z\right)^2 + \left(x - \frac{1}{2}wy\right)^2 - \left(\sqrt{b}\,w - \frac{1}{2}\frac{(1-a)z}{\sqrt{b}}\right)^2 - 2x^2 - \frac{5}{4}y^2 + \frac{1}{4b}(1-a)^2z^2 - \frac{1}{4}z^2 - \frac{1}{4}y^2w^2.$$

Let R_0 represent a sufficiently large region such that all trajectories, (x, y, z, w) satisfy $v(x, y, z, w) = R$ for $R > R_0$, under the following condition

$$2x^2 + \frac{1}{4}z^2 + \frac{1}{4}y^2w^2 + \frac{5}{4}y^2 + \left(\sqrt{b}\,w - \frac{1}{2}\frac{(1-a)z}{\sqrt{b}}\right)^2 > \left(x + \frac{1}{2}y\right)^2 + \left(y + \frac{1}{2}z\right)^2 + \left(x - \frac{1}{2}wy\right)^2 + \frac{1}{4b}(1-a)^2z^2$$

Consequently, on the surface defined by $\{(x, y, z, w) |\, v(x, y, z, w)\} = R$, and given that $R > R_0$, we can conclude that $v(x, y, z, w) < 0$. This implies that the set $\{(x, y, z, w) |\, v(x, y, z, w)\} \le R$ constitutes a bounded region for all trajectories of the system (1).

Other dynamical properties

For parameter $a = 4.01$, Fig. 3(a) and Fig. 3(b) present the LEs spectrum (LE_1, LE_2, LE_3, LE_4) in descending order and the Lyapunov dimension D_L (Kaplan-Yorke dimension DKY) as functions of parameter b within the range 0.4 to 0.6. The Wolf algorithm[53] computes the LEs using fourth-order Runge-Kutta integration with step size 0.005. To ensure results are free from transient effects and numerical artifacts, simulations extend to $t = 1 \times 10^8$. Computations are performed twice with slightly different initial conditions within the same basin of attraction and compared to verify accuracy.

From Fig. 3(a) can be seen that the maximum $D_L = 3.2455$ occurs at b = 0.4 with corresponding LEs: $LE_1 = 0.1301$, $LE_2 = 0.0000$, $LE_3 = 0.0000$ and $LE_4 = -0.5301$. With LEs signs (+, 0, 0, −), system (1) exhibits chaotic behavior with 2-torus characteristics.[51] Fig. 3(b) shows that decreasing the damping coefficient b increases D_L, reaching maximum value at $b = 0.4$. Further reduction in b leads to unbounded behavior.

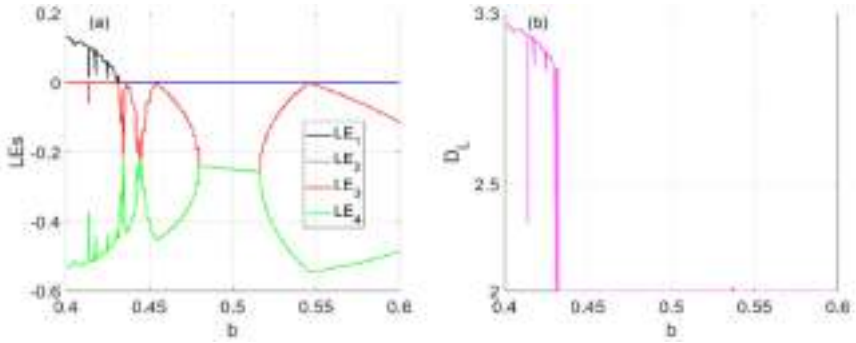

Fig. 3. LEs and D_L versus parameter b for a = 4.01.

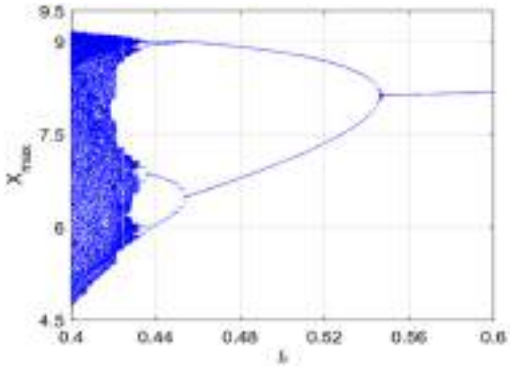

Fig. 4. Bifurcation diagram versus parameter b for a = 4.01.

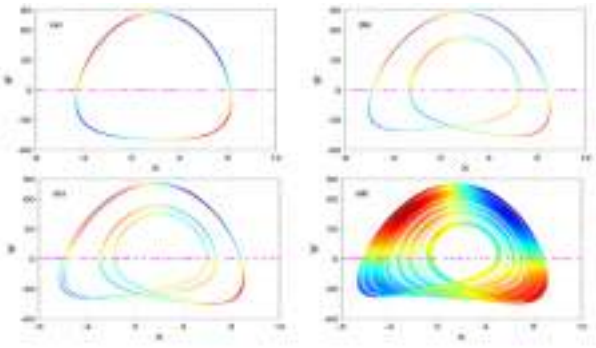

Fig. 5. Phase diagrams showing the period-doubling route to chaos with the initial condition (1.3, 1.77, 5.3, 1.08) *and* $b = 0.4$.

For $a = 4.01$, Fig. 4 shows the bifurcation diagram of the maximum x values (x_{max}) versus parameter b, which exposes a periodic-doubling route to chaos. Fig. 5 illustrates numerical trajectories for $b = 0.4$ with initial condition (1.3, 1.77, 5.3, 1.08) and parameter sequence $a = (4.6, 4.2, 4.12, 4.01)$, showing period-1, period-2, period-4 and chaotic behavior in the (x, w) plane. Pink dots indicate the infinite equilibrium line.

Multistability in the proposed system

This section explores multistability by analyzing the simultaneous presence of various attractors within the snap system (1).

Investigation of multistability

Multistability of the system (1) is tested, with $b = 0.4$, when bifurcation diagrams for x maxima (x_{max}) are presented in Fig. 6. The diagrams use forward (blue) and backward (magenta) continuations, with a bifurcation parameter range from 4 to 5. Forward continuation uses the provided initial conditions, while backward continuation uses the last iteration as initial conditions. Fig. 7 presents matching largest Lyapunov exponent (LLE) plots, including forward (blue) and backward (magenta) continuations. Several windows in the range $4 < a < 5$ detect multistable dynamics.

Coexisting hidden attractors

At $a = 4.2$, Fig. 8(a) shows coexisting period-2 (blue) and chaotic (magenta) hidden attractors from initial conditions (1.3, 1.77, 5.3, 1.08) and (1.5, 1.95, 5.3, 1.08), respectively. Fig. 8(b) demonstrates coexistence of period-2 (blue) and period-4 (magenta) hidden attractors at $a = 4.26$ with initial conditions (1.3, 1.77, 5.3, 1.08) and (1.5, 1.90, 5.3, 1.08). At $a = 4.45$, Fig. 8(c) shows coexisting period-2 (blue) and period-1 (magenta) hidden attractors from initial conditions (1.5, 1.75, 5.3, 1.1) and (1.3, 1.7, 5.3, 1.1). For a = 4.2 and b = 0.4, Fig. 9 shows four distinct basins of attraction evaluated at $z = w = 0$. The red basin corresponds to chaotic attractors, green to limit cycles (period-2 attractors), cyan to line equilibrium and yellow to divergent trajectories. The smooth basin boundaries between the limit cycle (green) and chaotic attractor (red) regions indicate that small changes in initial conditions can produce

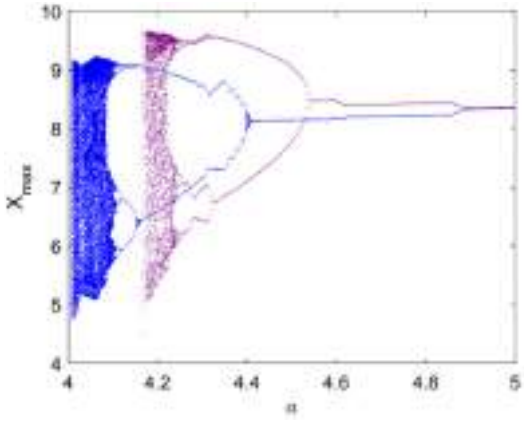

Fig. 6. Bifurcation diagrams using forward (blue) and backward (magenta) continuations for $b = 0.4$

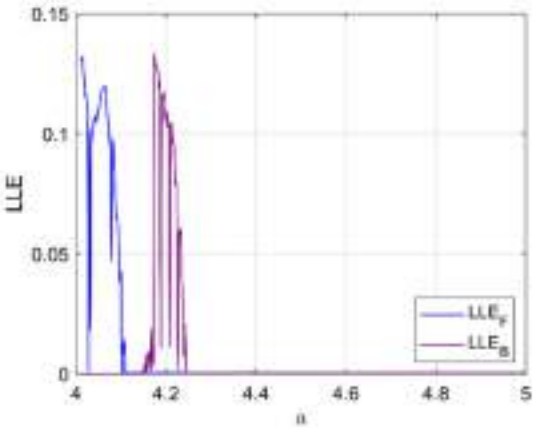

Fig. 7. Largest LEs corresponding to Fig. 6.

dramatically different final attractors. Fig. 10 reveals three dynamic regions on the $[a,\ b]$ parameter plane for initial conditions $(0.68,\ 1.12,\ -0.39,\ -0.13)$: red indicates hidden chaotic attractors, green represents periodic attractors and yellow shows divergent trajectories.

Amplitude and polarity control

This section examines mechanisms for controlling the amplitude and polarity of chaotic signals in the proposed snap system.

Control of chaotic signals

System (1) contains a single nonlinear term xy whose coefficient controls signal amplitude, as it is the only term with dimensions differing from the linear terms. Polarity control is achieved by introducing a constant in a variable x. The transformation $x \rightarrow m(x+n)$, $y \rightarrow my$, $z \rightarrow mz$, $w \rightarrow mw$, $t \rightarrow \frac{t}{m}$ converts system (1) to:

$$\begin{cases} \dot{x} = y, \\ \dot{y} = z, \\ \dot{z} = w, \\ \dot{w} = -az - bw - m\,(x+n)\,y. \end{cases} \tag{5}$$

In system (5), coefficient m controls the amplitude of all variables proportionally to $\frac{1}{m}$, while constant n provides polarity control, enabling transformation between bipolar and unipolar signals for variable x. Initial conditions require rescaling when amplitude and polarity parameters change due to the small basin of attraction. Unless stated otherwise, parameters are fixed at $a = 4.01$, $b = 0.4$ with initial conditions $(x,\ y,\ z,\ w) = \left(\frac{1}{m}\ (1.3\ -\ \mathrm{n},\ 1.77,\ 5.3,\ 1.08)\right)$.

Amplitude control of chaotic signals

At $n = 0$, Fig. 11 shows three chaotic signals from the system (5) for different amplitude controller values m. In Fig. 11(a), $m = 1$ produces high-amplitude chaotic signals (green), while $m = 2$ and $m = 5$ generate reduced amplitude signals (red and pink). Fig. 11(b) displays corresponding phase trajectories on the $(x,\ w)$ plane. Fig. 12(a) demonstrates that as an amplitude controller m varies from 1 to 5, the average absolute values of $|x|$, $|y|$, $|z|$ and $|w|$ scale inversely with m. Fig. 12(b) shows that the LEs spectrum remains unchanged because m affects only amplitude, not frequency.

Polarity control of chaotic signals

with $m = 5$, Fig. 13(a) presents three chaotic signals x from system (5) for different polarity controller values n. Fig. 13 (a) shows: negative unipolar signal (pink) for $n = 10$, bipolar signal (green) for $n = 0$ and positive unipolar signal (red) for $n = -10$. Fig. 13 (b) displays corresponding phase trajectories on the (x, w) plane for varying n values. Fig. 14(a) presents mean values of $x,\ y,\ z$ and w as functions of n. Parameter n affects only the mean value of x, leaving $y,\ z$ and w unchanged, confirming that n controls x polarity. Fig. 14(b) shows that LEs remain consistent across $-10 \leq n \leq 10$.As a result, changing n does not change the dynamics of the system but gives chaotic signals amplitude shift control, which is useful for applications that need particular signal polarities.

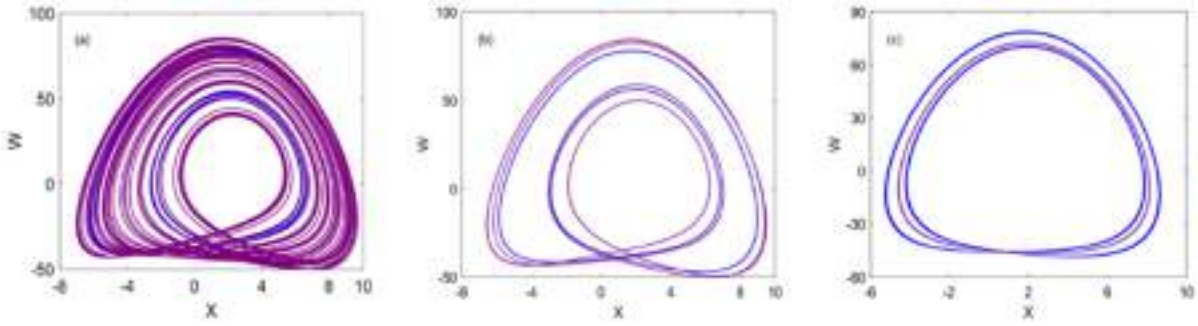

Fig. 8. Coexisting hidden attractors of the system (1) for b = 0.4: (a) $a = 4.2$, (b) $a = 4.26$, (c) $a = 4.45$.

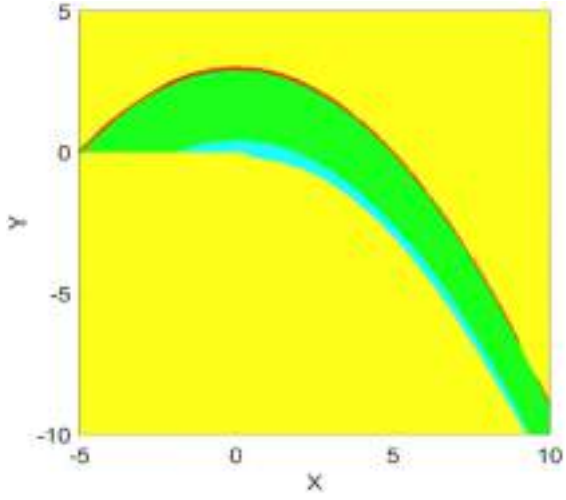

Fig. 9. Basin of attraction for the system (1) at w = 0, z = 0 with a = 4.2, b = 0.4.

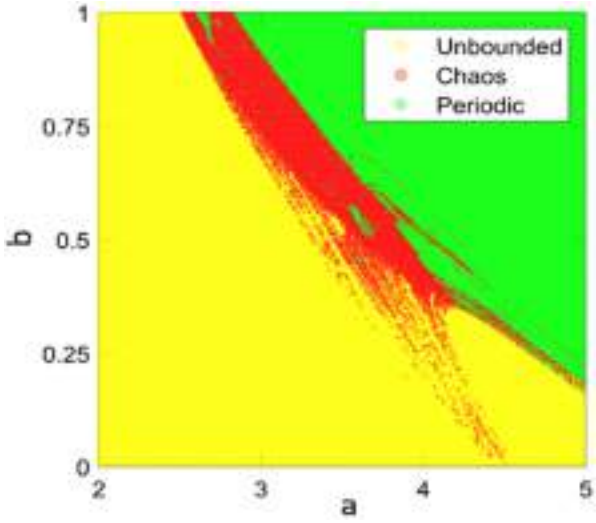

Fig. 10. Dynamic regions of the system (1) showing unbounded, periodic, and chaotic attractors on the [a, b] plane.

Self-reproducing system with infinitely many attractors

This section examines the self-reproducing system concept within the chaotic snap system framework, focusing on its capacity to generate infinite attractors.

Transformation to Self-reproducing system

Fig. 15 illustrates the process for generating infinite attractors. An endless lattice of chaotic attractors is created by transforming an offset boostable system into a self-reproducing one by incorporating periodic functions into a chaotic system. Trigonometric functions are commonly employed for constructing self-replicating systems.

Periodic offset boosting transforms an nD snap system into an (n − 1)D self-reproducing system.[31] Using $m = 1$ and $n = 0$, system (5) is modified to create a self-reproducing system in variables y, z and w, yielding a 3D lattice of infinitely many attractors:

$$\begin{cases} \dot{x} = f_2(y), \\ \dot{y} = f_3(z), \\ \dot{z} = f_4(w), \\ \dot{w} = -af_3(z) - bf_4(w) - xf_2(y), \end{cases} \tag{6}$$

where $f_2(y)$, $f_3(z)$ and $f_4(w)$ are periodic functions generating a 3D lattice of infinitely many hidden chaotic or periodic attractors. Variable x is not replaced with a periodic function because the cross-product term xy complicates finding suitable periodic replacements that preserve the system's dynamical behavior. Additionally, chaos vanishes when x is replaced with a periodic function.

Generation of infinitely many attractors

For parameters $a = 3.5$, $b = 0.4$, with periodic functions $f_2(y) = 2.5\ \sin(0.4y)$, $f_3(z) = 5\sin(0.2z)$ and $f_4(w) = 16\ \sin(0.0625w)$, system (6) exhibits an

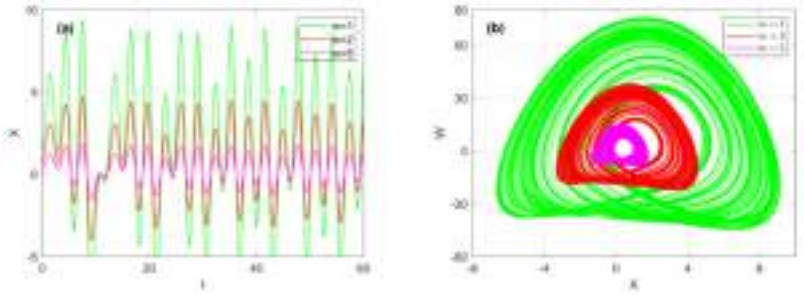

Fig. 11. Amplitude control of hidden chaotic attractors in the system (5): (a) Three chaotic signals (x) for different amplitude controller values m; (b) Phase trajectories for different m values.

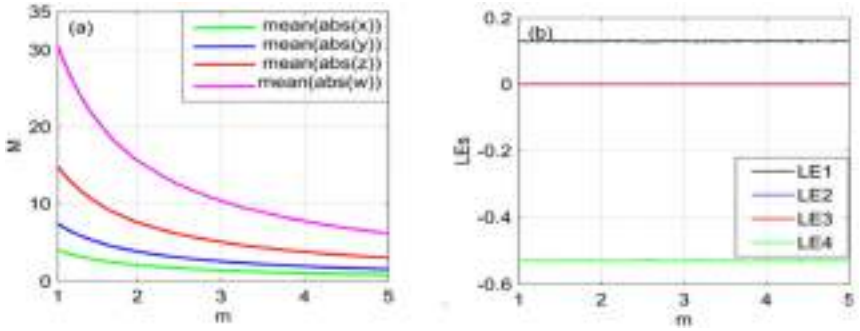

Fig. 12. Amplitude control analysis for system (5) with $m \in [1,\ 5]$: (a) Rescaled mean values of $|x|$, $|y|$, $|z|$ and $|w|$; (b) Invariant LEs spectrum.

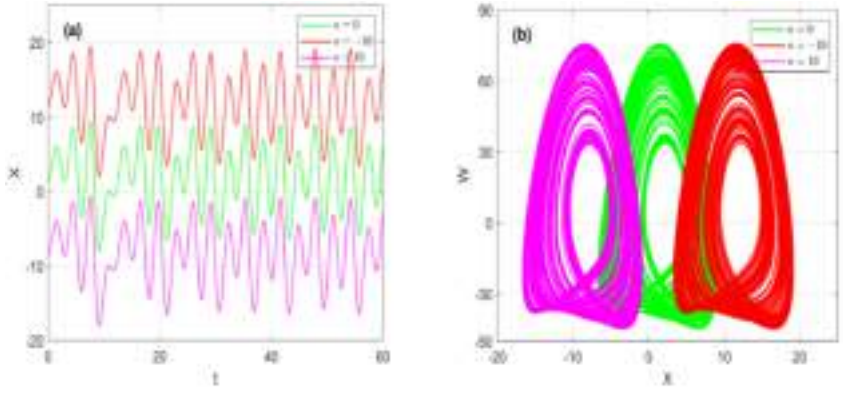

Fig. 13. Polarity control of hidden chaotic attractors in system (5) with m = 5: (a) Three chaotic signals (x) for different polarity controller values n; (b) Bipolar signal (green, n = 0), positive unipolar (red, n = −10) and negative unipolar (pink, n = 10).

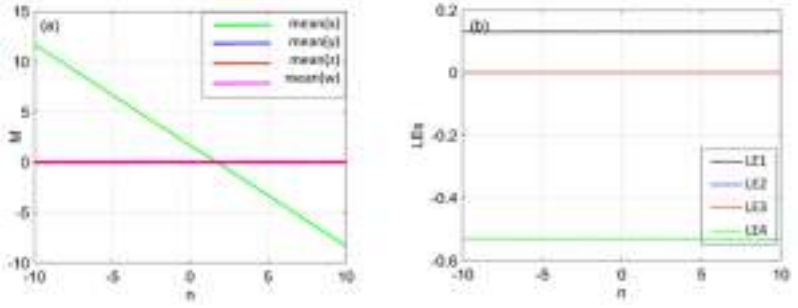

Fig. 14. Polarity control analysis for the system (5) with n ∈ [−10, 10]: (a) Mean values of signals x, y, z and w; (b) Invariant LEs.

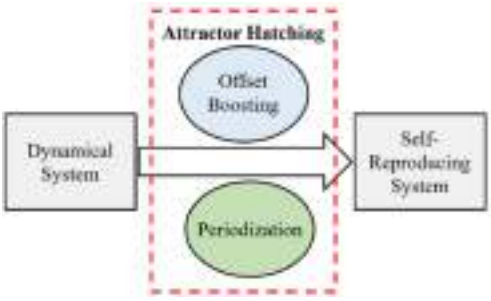

Fig. 15. Attractor generation process in a self-reproducing system.

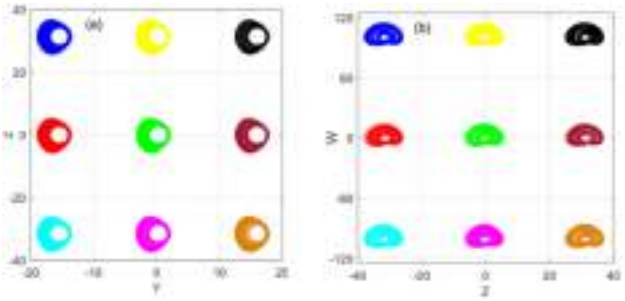

Fig. 16. 3D lattice of coexisting hidden chaotic attractors from system (6): (a) Initial conditions $(x_0,\ y_0,\ z_0,\ w_0) = (0.26,\ 0.35 + 5k\pi,\ 1.06 + 10k\pi,\ 0.22)$, (b) Initial conditions $(x_0,\ y_0,\ z_0,\ w_0) = (0.26,\ 0.35,\ 1.06 + 10k\pi,\ 0.22 + 32k\pi)$, with $k \in \{-1, 0, 1\}$.

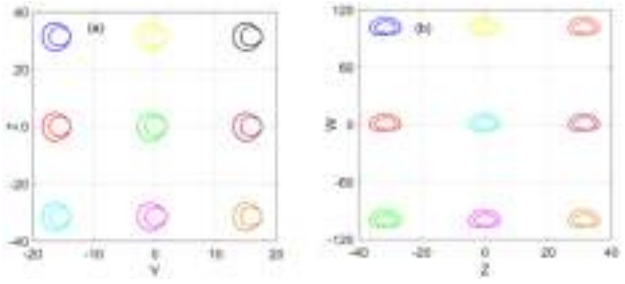

Fig. 17. 3D lattice of coexisting hidden periodic attractors from system (6): (a) Initial conditions $(x_0,\ y_0,\ z_0,\ w_0) = (0.26,\ 0.25+5k\pi,\ 1.3+10k\pi,\ 0.22)$, (b) Initial conditions $(x_0,\ y_0,\ z_0,\ w_0) = (0.26,\ 0.25,\ 1.3 + 10k\pi,\ 0.22 + 32k\pi)$, $with\ k \in \{-1, 0, 1\}$.

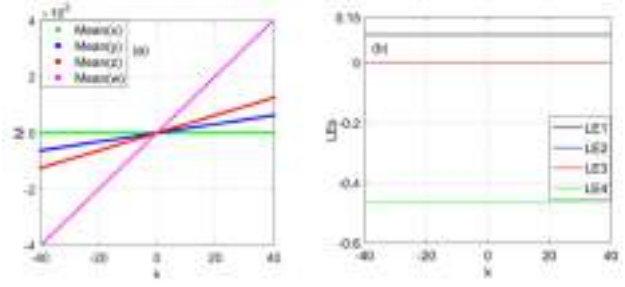

Fig. 18. Offset regulation of system (6) versus control parameter k from −40 to 40 for a = 3.5, b = 0.4: (a) Mean values with initial conditions $(0.26,\ 0.25 + 5k\pi,\ 1.06 + 10k\pi,\ 0.22 + 32k\pi)$; (b) Invariant LEs.

infinite 3D lattice of hidden chaotic and periodic attractors when initial conditions are selected according to the sinusoidal function periods.

Fig. 16 demonstrates that initial conditions $(x_0,\ y_0,\ z_0,\ w_0) = (0.26,\ 0.35 + 5k\pi,\ 1.06 + 10k\pi,\ 0.22)$ for the $(y,\ z)$ plane and $(x_0,\ y_0,\ z_0,\ w_0) = (0.26,\ 0.35,\ 1.06 + 10k\pi,\ 0.22 + 32k\pi)$ for the $(z,\ w)$ plane produces infinitely many hidden chaotic attractors with LEs $(0.0916,\ 0,\ 0,\ -0.4654)$ and Kaplan-Yorke dimension 3.1968.

Using initial conditions $(x_0,\ y_0,\ z_0,\ w_0) = (0.26,\ 0.25+5k\pi,\ 1.3+10k\pi,\ 0.22)$ for the $(y,\ z)$ plane and $(x_0,\ y_0,\ z_0,\ w_0) = (0.26,\ 0.25,\ 1.3+10k\pi,\ 0.22+32k\pi)$ for the $(z,\ w)$ plane, as shown in Fig. 17 system (6) generates infinitely many hidden periodic attractors with LEs $(0,\ 0,\ -0.0710,\ -0.3065)$ and Kaplan-Yorke dimension 2.0.

As illustrated in Fig. 18, since the periods of $\sin(0.4y)$, $\sin(0.2z)$ and $\sin(0.0625w)$ are $5k\pi$, $10k\pi$ and $32k\pi$, respectively, the initial conditions of y, z and w vary according to k; their offsets are modulated, while the average value of x remains unchanged. Notably, the LEs $(LE_1,\ LE_2, LE_3,\ LE_4)$ remains relatively unchanged for $-40 \le k \le 40$.

Hardware implementation using STM32 microcontroller

Digital implementation of chaotic systems provides substantial advantages over analog approaches, including precise control of initial conditions and reduced sensitivity to parasitic effects. The proposed 4D chaotic system is implemented with this STM32F103ZET6 microcontroller as the hardware realization. The STM32F103ZET6 is built with an ARM Cortex-M3 core that runs at 72 MHz with 512 KB Flash memory and 64 KB SRAM. The microcontroller has dual 12-bit Digital-to-Analog Converters (DACs) for direct raw analog chaotic signal generation, with no additional conversion on the outside. The integrated DAC functionality allows the hardware design to be less complicated while preserving signal fidelity. The digital implementation involves discretizing the continuous 4D system described in Eq. (1). As the computational efficiency is high and embedding the algorithm is easy, the Euler method is chosen. The formulas that are discretized are:

$$\begin{cases} x[n+1] = x[n] + dt \times y[n], \\ y[n+1] = y[n] + dt \times z[n], \\ z[n+1] = z[n] + dt \times w[n], \\ w[n+1] = w[n] + dt \\ \quad \times (-az[n] - bw[n] - x[n]y[n]), \end{cases} \tag{7}$$

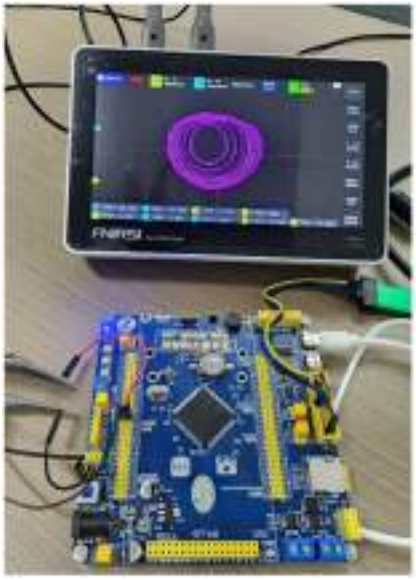

Fig. 19. Experimental platform for 4D chaotic system (1) hardware implementation based on STM32.

where dt represents the integration step size and n denotes the discrete time index.

The system provides periodic timer-based interruption service scheduling at 10 kHz to enable temporal convergence. Repeated iterations of the discretized equations are computed at each interrupt, permitting the attainment of a simulation of an effective frequency of 100 kHz; this promotes a nice, smooth chaotic structure suitable for monitoring on an oscilloscope. Fig. 19 presents an experimental setup of the platform. The chaotic variables are scaled to the 12-bit DAC range (0-4095) and sent via DAC channels PA4 and PA5. Scaling parameters are determined from observed dynamic ranges: $x \in [-10, 10]$, $y \in [-18, 12]$, $z \in [-26, 26]$and $w \in [-45, 80]$.

The experimental validation work uses an FNIRSI 1013D digital oscilloscope (100 MHz bandwidth, with 1 GS/s sampling rate). The oscilloscope runs in XY mode to view the chaotic attractor phase portrait visualization. The experimental traces on the $x-y$, $x-z$ and $x-w$ planes using the parameter values yielding the highest LEs and Lyapunov dimension D_L picked out at those parameters a = 4.01, b = 0.4 and integration step $dt = 0.01$ are illustrated in Fig. 20(a),(b) and (c), respectively. The trajectories of the experiments show excellent correspondence with the numerical simulations shown in Fig. 2. The implementation here demonstrates that by adopting a microcontroller-based realization approach to design, a cost-effective, adaptable solution can be found for the deployment of a chaotic system.

Design of RNG algorithm and NIST test

Inherent to the encryption process, security requires the use of random bit sequences. Therefore, chaotic systems are frequently utilized in random number generation (RNG) due to their complex dynamics. This RNG design employs the chaotic system described in Eq. (1), with parameters $a = 4.01$ and $b = 0.4$. Initial conditions are $(x(0), y(0), z(0), w(0)) = (1.3, 1.77, 5.3, 1.08)$ for hidden chaotic attractors. The design steps of the RNG algorithm are shown in Algorithm 1, which is summarized as follows:

1. Initialize the chaotic system (1) with specified initial conditions and system parameters.
2. Set sampling interval $h = 0.01$.
3. Integrate the chaotic system using the RK4 algorithm.
4. Extract float values from the system at each sampling interval.
5. Convert float values to 32-bit binary representation.
6. Extract the 4 least significant bits (LSB) from phase variables x, y, z and w appending these to the random number sequence.
7. Repeat steps until a 1-million-bit sequence is generated.
8. Apply NIST tests to the 1-million-bit sequence. Tests are considered successful when resultant \$P\$-values exceed 0.001.

RNG method validation uses the widely used statistical test suite NIST SP 800 – 22, a protocol

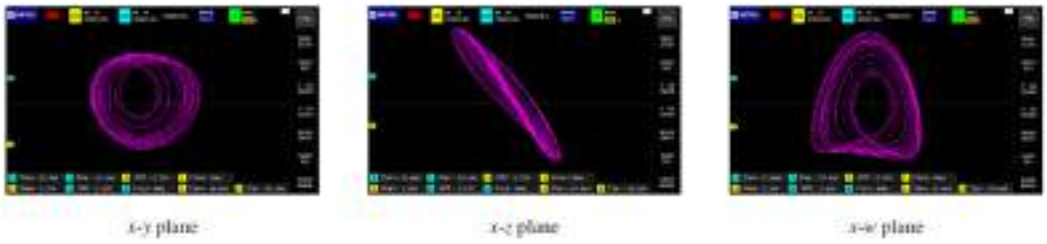

Fig. 20. Experimental phase portraits from STM32 implementation for parameters a = 4.01, b = 0.4: (a) x-y plane, (b) x-z plane, (c)x-w plane.

Algorithm 1 Pseudo Code for RNG Design Algorithm using Chaotic System.

Input: Chaotic system parameters: $a = 4.01,\ b = 0.4$
Initial conditions: $x(0) = 1.3,\ y(0) = 1.77,\ z(0) = 5.3,\ w(0) = 1.08$
Output: Random bit sequences for x, y, z, w
Set sampling interval $h = 0.01$
Initialize bit counts: $n_x = 0$, $n_y = 0$, $n_z = 0$, $n_w = 0$
Initialize bit sequences: rng-x, rng-y, rng-z, rng-w
While ($n_x < 10^6$ or $n_y < 10^6$ or $n_z < 10^6$ or $n_w < 10^6$)
    Integrate the chaotic system using RK4 over the interval h
    Extract state variables $x,\ y,\ z,\ w$ at time $t + h$
    Convert $x,\ y,\ z,\ w$ to a 32-bit binary representation
    if $n_x < 10^6$ **then**
        rng-x = [rng-x, Extract 4 LSB of x]
        $n_x = n_x + 4$
    end if
    if $n_y < 10^6$ **then**
        rng-y = [rng-y, Extract 4 LSB of y]
        $n_y = n_y + 4$
    end if
    if $n_z < 10^6$ **then**
        rng-z = [rng-z, Extract 4 LSB of z]
        $n_z = n_z + 4$
    end if
    if $n_w < 10^6$ **then**
        rng-w = [rng-w, Extract 4 LSB of w]
        $n_w = n_w + 4$
    end if
end while
Verify every bit sequence using the NIST SP 800-22 test suite.
Evaluate test results for rng-x, rng-y, rng-z, rng-w
if All tests pass for all sequences, **then**
    return valid random bit sequences for $x,\ y,\ z,\ w$
else
    return Failure: adjust parameters or initial conditions
end if

benchmark for randomness testing. This package includes 15 test sets, such as monobit, runs, and binary matrix rank tests. Numbers generated from outputs x, y, z and w passed all tests. Results specific to outputs x, y, z and w are given in Table 3. RNG outputs that pass all NIST SP 800-22 tests are considered secure for high-security applications, including encryption and data protection. System (1) passed the NIST SP 800-22 test suite successfully, as shown in Table 3.

Application to image encryption

As shown in the previous section (see Table 3), system (1) with $a = 4.01$, $b = 0.4$ and initial conditions (1.3, 1.77, 5.3, 1.08), corresponding to hidden chaotic attractors, is successfully passed by the NIST SP 800-22 test suite, demonstrating its suitability for cryptographic applications. This section presents the feasibility of the system (1) in the context of chaos-based image encryption, wherein the following encryption algorithm, specifically designed for grayscale images, is employed.

A.1 Import the plain image $P_{M\times N}$ and represent it as a matrix of size $M \times N$, where M and N correspond to the height and width of the image, respectively.
A.2 Compute the image-dependent perturbation constant $\mathrm{Img_C}$:

$$\mathrm{Img_C} = \frac{1}{M \times N} \sum_{l=1}^{M} \sum_{K=1}^{N} P(l,k),$$

Table 3. RNG NIST-800-22 test results for binary sequences of x, y, z, and w.

Test Item	P-value (x)	P-value (y)	P-value (z)	P-value (w)	Result
Approximate Entropy	0.25955	0.80481	0.27654	0.58981	Passed
Block Frequency	0.86009	0.42527	0.60142	0.75601	Passed
Cumulative Sums	0.62739	0.64391	0.61374	0.83674	Passed
FFT	0.50292	0.72730	0.29128	0.21882	Passed
Frequency	0.68327	0.97287	0.38649	0.92193	Passed
Linear Complexity	0.39572	0.24806	0.42335	0.55272	Passed
Longest Run	0.75867	0.64663	0.24996	0.97391	Passed
Nonoverlapping Template	0.57482	0.09558	0.17051	0.80806	Passed
Overlapping Template	0.58508	0.16877	0.38738	0.14876	Passed
Random Excursions ($x = 4$)	0.42895	0.20870	0.72364	0.55470	Passed
Random Excursions Variant ($x = 4$)	1.00000	0.15332	0.98585	0.24469	Passed
Ranks	0.42832	0.97554	0.92685	0.21424	Passed
Runs	0.28021	0.42952	0.01346	0.45687	Passed
Serial Test	0.13945	0.10047	0.41061	0.03597	Passed
Maurer's Universal	0.14165	0.58046	0.02725	0.70830	Passed

where l and k denotes the coordinates of a pixel in the image P.

A.3 Add the value of $\mathrm{Img_C}$ into a selected system parameter like, i.e., b, as a perturbation value that will allow the image P to affect the calculation of the secret key. Throwing away the transient states will allow you to achieve the state sequences: $x(i), y(i), z(i), w(i),\ i = 1, 2, \ldots, n$, where $n = M \times N$, where x, y, z and w denote the system's state variables which will then be used in key generation as well as pixel permutation.

A.4 Construct the secret key and permutation sequences using the system states:

$$k_s = \mathrm{mod}\left(\lfloor x(i) \times 10^{15} \rfloor,\ 256\right),$$

$$\mathrm{row} = \mathrm{mod}\left(\lfloor y(i) \times 10^{15} \rfloor,\ 256\right) + 1$$

$$\mathrm{col} = \mathrm{mod}\left(\lfloor z(i) \times 10^{15} \rfloor,\ 256\right) + 1$$

The key sequence k_s is constrained to $[0, 255]$, matching the grayscale pixel range. The sequences row and col define the mapping for pixel shuffling, bounded within $[1, 256]$, ensuring valid matrix indexing.

A.5 Create Row(j) and Col(j), which define new pixel locations, by choosing the first 256 distinct elements from the generated sequences. The permutation process iteratively maps each Row(j) to all sorted Col(j) values, covering the full image matrix while preserving pixel intensities.

A.6 Reshape the one-dimensional key vector k_s into a matrix matching the image dimensions:

$$K_s = reshape\left(k_s, M, N\right),$$

facilitating element-wise encryption operations.

A.7 Shuffle the plain image pixels according to the established mapping:

$$P_{shf}(i, j) = P\left(\mathrm{Row}(j),\ \mathrm{Col}(j)\right)$$

resulting in a rearranged intermediate image P_{shf} that obscures spatial correlations.

A.8 Obtain the encrypted image P_{enc} by performing a bitwise XOR operation between K_s and P_{shf}:

$$P_{enc}(i, j) = P_{shf}(i, j) \oplus K_s(i, j).$$

To recover the plain image, the steps below are followed:

D.1 Apply XOR between the P_{enc} and K_s to retrieve the P_{dec}: $P_{dec}(i,\ j) = P_{enc}(i,\ j) \oplus K_s(i,\ j)$.

D.2 Reverse the pixel permutation to obtain the original image:

$$P_{dshf}\left(Row(i),\ Col(j)\right) = P_{dec}(i,\ j),$$

yielding P_{dshf}, which is identical to the original P image.

The flowchart of the aforementioned algorithm for the image encryption and decryption scheme is illustrated in Fig. 21. The aforementioned algorithm is applied to the system (1) with $a = 4.01,\ b = 0.4$ and initial conditions $(1.3,\ 1.77,\ 5.3,\ 1.08)$, using the Boat, Clock, and Lena images of size $M = N = 256$. The plain, shuffled, encrypted, and decrypted images are illustrated in Fig. 22.

Security analysis results

The reliability of the proposed image encryption approach based on system (1) is evaluated through a series of standard security analyses, including key space exploration, histogram analysis, pixel correlation evaluation, differential and cropping attack

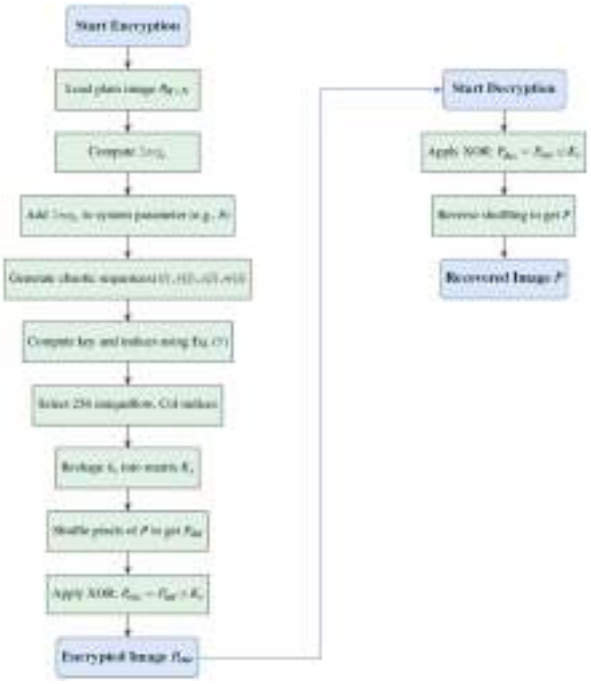

Fig. 21. Flowchart of the image encryption and decryption algorithm.

resistance and information entropy assessment. The calculated perturbation constants Img_c for the Boat, Clock and Lena images are 3.0201×10^{-8}, 4.3302×10^{-8} and 2.9150×10^{-8}, respectively.

Key Space Analysis: The robustness of an encryption system is largely dependent on the breadth and structure of its key space. To effectively resist brute-force attacks, it must typically be ensured that the key space exceeds 2^{128}, making any exhaustive search attempts computationally infeasible.[54,55] The secure key is based on the set $\{a,\ b, (x_0, y_0, z_0, w_0),\ Img_C\}$, with each parameter represented in double precision. Considering that the calculation precision is approximately 10^{-15}, when calculated using 64-bit double-precision arithmetic, the total key space is estimated to be on the order of 10^{-15} which greatly surpasses the widely recognized minimum threshold for secure encryption.

Histogram Analysis: One method for evaluating the encryption scheme's resistance to statistical attacks is histogram analysis. The number of pixels that correspond to each gray level is shown to illustrate the frequency distribution of pixel intensities. A nearly uniform histogram is generally considered a hallmark of an effective encryption algorithm. In this study, histogram evaluations are conducted on the Boat, Clock, and Lena images, as well as on their respective shuffled and encrypted counterparts. The resulting distributions for the original, shuffled, and ciphered images are depicted in Fig. 23. It can be observed that the histogram of the encrypted image is uniformly distributed and is completely different from that of the original image, which demonstrates the effectiveness of the encryption method in obscuring the statistical structure of the image. The variance is calculated as follows.[56]

$$Var\,(h) = \frac{1}{G^2}\sum_{i=0}^{G-1}\sum_{j=0}^{G-1}\frac{1}{2}\,(h_i - h_j)\,,$$

where $G = 256$ is the number of grey levels and h is the vector of the histogram value. The histogram variances of both the plain and encrypted images, along with the corresponding percentage reductions for the Boat, Clock, and Lena images, are presented in Table 4. It is demonstrated that encryption substantially decreases the variance compared to the original images, highlighting the effectiveness of the proposed scheme based on the system (1).

Pixel Correlation Analysis: The examination of pixel correlation is a standard technique that may be used by attackers to analyze and potentially breach cryptosystems. In natural images, strong correlations are typically exhibited by adjacent pixels in all directions—horizontal, vertical and diagonal. Therefore, it is expected that a robust encryption scheme will significantly reduce the correlation between neighboring pixels in the ciphered image, enhancing resistance against statistical attacks. The correlation coefficient is defined as follows:[55]

$$r_{XY} = \frac{cov\,(X, Y)}{\sqrt{\sigma_X\ \sigma_Y}},$$

where the covariance is given by: $cov(X, Y) = \mathrm{E}[(\mathrm{X} - \mathrm{E(X)})(\mathrm{Y} - \mathrm{E(Y)})\,] = \frac{1}{N}\sum_{i=1}^{N}(X_i - \mathrm{E(X)})(Y_i - \mathrm{E(Y)})$, and X and Y represent the grayscale values of two adjacent pixels in the image, where $E(X) = \frac{1}{N}\sum_{i=1}^{N} X_i$ and $\sigma_X = \frac{1}{N}\sum_{i=1}^{N}(X_i - \mathrm{E(X)})^2$. The values of correlation between two adjacent pixels in the vertical, horizontal and diagonal directions of the original and encrypted images for the Boat, Clock and Lena images are presented in Table 5. It is shown that the correlation coefficients for the encrypted images are very close to zero, indicating that statistical dependencies between adjacent pixels are effectively eliminated by the proposed encryption algorithm for system (1).

Differential Attack: Two metrics are commonly used to evaluate the robustness of an encryption scheme against differential attacks: the "Number of Pixels Change Rate" (NPCR) and the "Unified Average

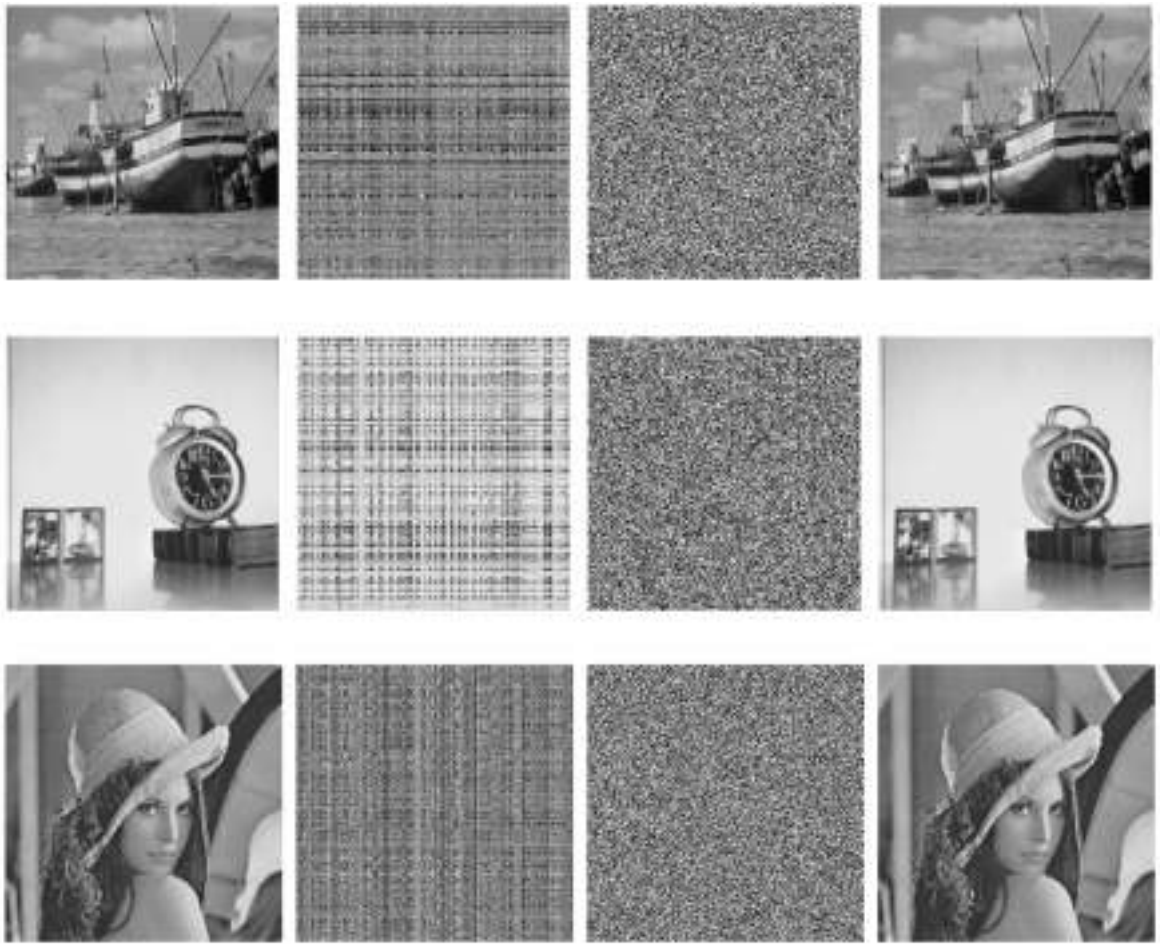

Fig. 22. From left to right, the columns represent the original image, the image after pixel shuffling, the encrypted image and the decrypted image.

Changing Intensity" (UACI). These metrics quantify the effect of minor modifications in the original image on the resulting encrypted image. In this approach, the encryption process is analyzed by introducing small changes in the input, either by flipping specific bits or by using randomly selected bits and by observing the resulting differences in the ciphered images. A measure of the proportion of pixels that differ between two encrypted images and the average intensity variation caused by these changes is provided by NPCR and UACI, respectively, as described in.[57] The formulas are defined as follows:

$$\text{NPCR}(\%) = \frac{1}{M \times N} \sum_{i=1}^{M} \sum_{j=1}^{N} \left| sign\left(C_1(i,j) - C_2(i,j)\right) \right| \times 100$$

$$\text{UACI}(\%) = \frac{1}{M \times N} \sum_{i=1}^{M} \sum_{j=1}^{N} \frac{\left|C_1(i,j) - C_2(i,j)\right|}{255} \times 100$$

where C_i denotes the encrypted image and sign() is the standard sign function. In an ideal encryption scenario, it is expected that the NPCR should approach 100%, while the UACI is expected to be around 33.33%. As shown in Table 6, the NPCR and UACI results of three sample images with the proposed encryption scheme for system (1) are close to the ideal values, demonstrating strong sensitivity to changes in image pixels and mismatched keys.

Information Entropy: Information entropy analysis is used to quantify the randomness or unpredictability present in encrypted data. It is required that an effective encryption algorithm produces ciphered data that is highly random, preventing any meaningful inference about the original image. Entropy can be formally defined as:

$$H(S) = \sum_{i=0}^{2^N-1} p_i \log_2 \frac{1}{p_i},$$

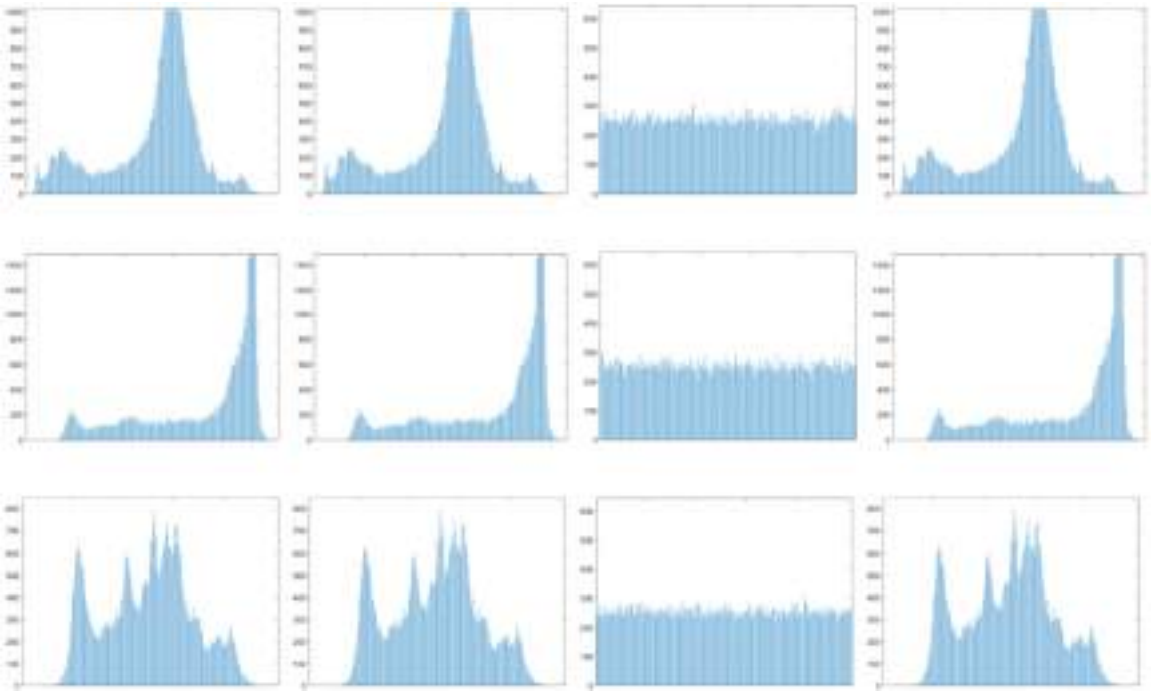

Fig. 23. The histogram distribution: the first column shows the original image, the second column shows the image after shuffling, the third column shows the encrypted image and the fourth column shows the decrypted image. The first to third rows correspond to the Boat, Clock and Lena images, respectively.

Table 4. Histogram variances of the original and encrypted images, along with the corresponding percentage reductions, for the Boat, Clock and Lena images, respectively.

Image	Plain	Encrypted	Reduction (%)
Boat	101070	290.9255	99.7122
Clock	283170	292.9176	99.8966
Lena	49027	246.3529	99.4975

Table 5. Correlation coefficients between adjacent pixels in the horizontal, vertical, and diagonal directions for the original and encrypted images.

Image	Type	Horizontal	Vertical	Diagonal
Boat	Original	0.9267	0.9449	0.8833
	Encrypted	−0.0006	−0.0018	−0.0027
Clock	Original	0.9566	0.9743	0.9393
	Encrypted	0.0004	0.0006	0.0004
Lena	Original	0.9635	0.9806	0.9431
	Encrypted	−0.0006	−0.0079	−0.0013

Table 6. Results for NPCR and UACI, evaluated according to the approach described in,[57] are presented.

Image	NPCR (%)	UACI (%)
Boat	99.6185	33.3056
Clock	99.5895	33.4497
Lena	99.5743	33.3771

Table 7. Entropy values for the plain, shuffled and encrypted images of the Boat, Clock and Lena.

Image	Plain	Shuffled	Encrypted
Boat	7.1587	7.1587	7.9968
Clock	6.7057	6.7057	7.9968
Lena	7.3509	7.3509	7.9973

where $H(S)$ denotes the entropy, S represents an input symbol and p_i corresponds to the probability of the i^{th}symbol. For a truly random grayscale image, the entropy value should ideally be 8. The calculated entropy values for the encrypted Boat, Clock and Lena images are presented in Table 7 Since these values are very close to 8, a high level of randomness and a very low probability of information leakage are indicated.

Cropping Attack: To test the encryption scheme against cropping attacks, selected 256 × 75 blocks of the encrypted image are set to black. The encrypted and decrypted Boat images are illustrated in Fig. 24. Although some data was lost, the decrypted image is still visually identifiable, confirming the robustness of the encryption scheme based on system (1).

The results summarized in Tables 4 to 7 provide comprehensive evidence of the encryption performance of the proposed system (1). The substantial reduction in histogram variance is demonstrated by the nearly uniform intensity distributions exhibited

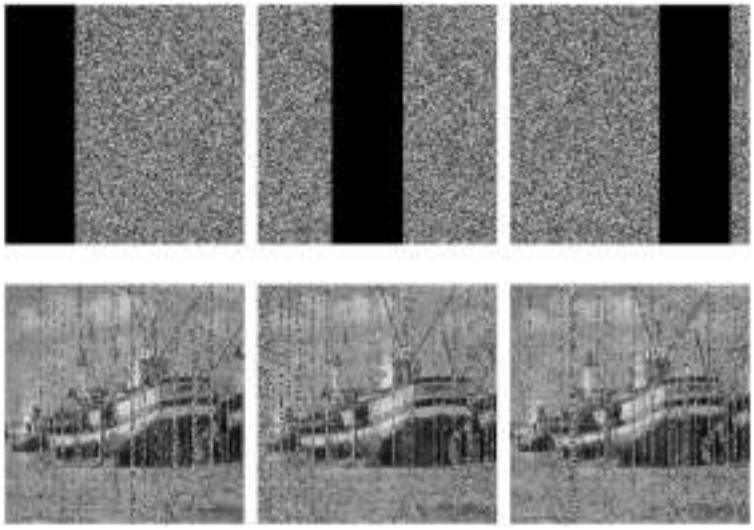

Fig. 24. Cropping attack for Boat image.

by the encrypted images, confirming strong diffusion characteristics. The near-zero correlation coefficients between adjacent pixels indicate that statistical dependencies in the cipher images have been effectively eliminated. Furthermore, entropy values of approximately 7.99 are reported, which are very close to the theoretical maximum of 8, highlighting the high randomness and information uncertainty of the encrypted data. Finally, NPCR and UACI values exceeding 99% and approaching 33%, respectively, are reported to satisfy the well-established benchmarks for secure and robust image encryption.

Conclusions and discussion

In this paper a simple six-term chaotic snap system with a line of equilibria and a single quadratic nonlinear term is presented. The proposed system has several considerable advantages compared to existing chaotic snap systems. It provides reduced algebraic difficulty, with six terms as opposed to seven or eight used in previous systems. It includes only one quadratic nonlinearity rather than more nonlinear terms. It also has a higher LE_1 value, showing greater system instability and a higher Lyapunov dimension D_L, which represents complicated fractal structure at attractor basin boundaries. The dissipative behavior is evident for $b > 0$ and conservative for $b = 0$. With integrated and hidden attractors, this system is multistable in the dissipative case. Based on numerical simulations, the system can support both chaotic attractors as well as periodic limit cycles, where the behavior highly sensitive with the initial state. The system exhibits a coherent multistable dynamics as evidenced by the fact that the basin boundaries among coexisting attractors demonstrate smooth fractal structures.

One unique feature of system (1) is the accurate amplitude modulation capability achieved by the quadratic nonlinearity coefficient and thus provides efficient signal power control. As a basic function, the system contains the polarity control mechanism for the x-variable, as well as introducing a constant to the x-variable which generates the chaotic signal with opposite polarities. By using periodic functions, the system turns into self-propagating form and produces 3D lattices of hidden attractors without changing the value of LEs. It allows producing chaotic signals having polarity through the initial condition selection. As a result, it is the most basic configuration having all these properties.

The realization based on STM32 and great agreement with the numerical simulation shown in experimental phase portraiture indicates that the solution is practical. Real-time chaotic signals suitable for oscilloscope observation are successfully generated by the system, validating its effectiveness for practical applications. The strong potential of the system for chaos-based secure communication and cryptographic applications is demonstrated by the NIST SP 800 22 statistical tests. The validation criteria are successfully passed by all generated random number sequences, confirming their suitability for secure communication and cryptographic purposes. Furthermore, the feasibility of chaos-based security has been verified through the successful implementation of the proposed system (1) in image encryption. Future research directions include theoretical investigations such as qualitative theory, synchronization studies and fractional-order dynamics.

Acknowledgments

The authors sincerely thank the reviewers and the editor for their valuable comments and suggestions, which improved the quality of this paper.

Authors' declaration

- Conflicts of Interest: None.
- We hereby confirm that all the Figures and Tables in the manuscript are ours. Furthermore, any Figures and images that are not ours have been included with the necessary permission for republication, which is attached to the manuscript.
- No animal studies are present in the manuscript.
- No human studies are present in the manuscript.
- Ethical Clearance: The project was approved by the local ethical committee at Soran University.

Authors' contributions statement

This research was carried out through the collaborative efforts of all authors. S.H.M. contributed to conceptualization, validation, investigation, and writing of the original draft. I.A. and R.H.S. contributed to the conceptualization and methodology, supervised the research process, and contributed to the editing of the manuscript. All authors have read and approved the final version of the manuscript.

References

1. Lorenz EN. Deterministic Nonperiodic Flow. J Atmos Sci. 1963;20(2):130–141.https://doi.org/10.1175/1520-0469(1963)020<0130:DNF>2.0.CO;2.
2. Abdulrazaq ZA, Ayoub HG, Zaidan H. Synergistic Construction of High-Performance S-Boxes Based on Chaotic Systems: A Paradigm Shift in Cryptographic Security Design. Chaos and Fract. 2025;2(2):43–49. https://doi.org/10.69882/adba.chf.2025073
3. Jiang Z, Yan W, Ding W, Yue L, Ding Q. SM4 Chaotic masking scheme against power analysis based on FPGA. Int. J. Bifurcat. Chaos. 2022;32(08):2250110. https://doi.org/10.1142/S0218127422501103.
4. Benkouider K, Mahdal M, Vaidyanathan S, Tlelo-Cuautle E, Martínez BO, Kaçar S, *et al.* FPGA implementation and voice encryption application of a new hyperchaotic system with high complexity. Sci Rep. 2026;16:4485. https://doi.org/10.1038/s41598-025-34605-z
5. Matsumoto T, Chua L, Komuro M. The double scroll. IEEE Trans Circuits Syst. 1985;32(8):797–818. https://doi.org/10.1109/TCS.1985.1085791.
6. Rasul TI, Salih RH. Hopf Bifurcation of Three-Dimensional Quadratic Jerk System. Baghdad Sci J. 2024;21(7):2378. https://doi.org/10.21123/bsj.2023.8945.
7. Li C, Akgul A, Bi L, Xu Y, Zhang C. A chaotic jerk oscillator with interlocked offset boosting. Eur Phys J Plus. 2024;139(3):1–10. https://doi.org/10.1140/epjp/s13360-024-05040-2.
8. Lăzureanu C. The Cusp Bifurcation of a Jerk System. Int. J Bifurcat Chaos. 2024;34(10):2450126. https://doi.org/10.1142/S0218127424501268.
9. Llibre J, Sun X. Small-amplitude periodic solutions in the polynomial jerk equation of arbitrary degree. Phys D Nonlinear Phenom. 2025;476:134628. https://doi.org/10.1016/j.physd.2025.134628.
10. Zhang J, Li G, Pan H, Chen X. Multi-Scroll Expansion of 3D and 4D Jerk Systems and its DSP Implement. Chinese J Phys. 2025;94:627–49. https://doi.org/10.1016/j.cjph.2025.02.002.
11. Li B, Sang B, Liu M, Hu X, Zhang X, Wang N. Some jerk systems with hidden chaotic dynamics. Int. J. Bifurcat. Chaos. 2023;33(06):2350069. https://doi.org/10.1142/S0218127423500694.
12. Vivekanandan G, Kengne LK, Chandrasekhar D, Fozin TF, Minati L. Interior Crisis Route to Extreme Events in a Memristor-Based 3D Jerk System. Int J Bifurcat Chaos. 2024;34(13):2450161. https://doi.org/10.1142/S021812742450161X.
13. Chlouverakis KE, Sprott J. Chaotic hyperjerk systems. Chaos Solit Fract. 2005;28(3):739–46. https://doi.org/10.1016/j.chaos.2005.08.019 .
14. Vaidyanathan S, Hannachi F, Mohamed MA, Sambas A, Aruna C, Ramesh R. A new chaotic hyperjerk system with a half-line of equilibrium points, its dynamic analysis, multistability, circuit simulation and anti- synchronization via backstepping control. Arch Control Sci. 2025;35(1):123–143. https://doi.org/10.24425/acs.2025.153960.
15. Sambas A, Miroslav M, Vaidyanathan S, Ovilla- Martínez B, Tlelo-Cuautle E, Abd El-Latif AA, Abd-El-Atty B, Benkouide K, Bonny T. A new hyperjerk system with a half line equilibrium: Multistability, period doubling reversals, antimonotonocity, electronic circuit, FPGA design, and an application to image encryption. IEEE Access. 2024;12:9177–94. https://doi.org/10.1109/ACCESS.2024.3351693.
16. Kengne R, Talla Mbe J, Fotsing J, Mezatio AB, Ntsafack Manekeng FJ, Tchitnga R. Dynamics and synchronization of a novel 4D-hyperjerk autonomous chaotic system with a Van der Pol nonlinearity. Z Naturforsch A. 2023;78(9):801–21. https://doi.org/10.1515/zna-2023-0063.
17. Rong X, Chedjou JC, Yu X, Shukhratovich MB, Jiang D, Kengne J. A special memristive diode-bridge-based hyperchaotic hyperjerk autonomous circuit with three positive Lyapunov exponents. Chaos Solit Fract. 2024;189(1):115704. https://doi.org/10.1016/j.chaos.2024.115704.
18. Wang R, Li C, C Çiçek S, Rajagopal K, Zhang X. A memristive hyperjerk chaotic system: amplitude control, FPGA design, and prediction with artificial neural network. Complexity. 2021;2021(1):6636813. https://doi.org/10.1155/2021/6636813.
19. Wang H,Wang L, Lian X. Memristive Chaotic Circuit Designed for Image Encryption. In: 2024 9th International Conference on Integrated Circuits and Microsystems (ICICM). IEEE; 2024;702–706. https://doi.org/10.1109/ICICM63644.2024.10814402.
20. Llibre J, Valls C. On the dynamics of a hyperjerk memristive system. Appl Phys A. 2024;130(11):903. https://doi.org/10.1007/s00339-024-08073-7.
21. Joshi M, Mohit P, Ranjan A. n-th-Order Simple Hyperjerk System with Unstable Equilibrium and Its Application as RPG. Circuits Syst Signal Process. 2021;40:5913–5934. https://doi.org/10.1007/s00034-021-01752-3.

22. Zambrano-Serrano E, Anzo-Hernández A. A novel antimonotic hyperjerk system: Analysis, synchronization and circuit design. Phys D Nonlinear Phenom. 2021;424:132927. https://doi.org/10.1016/j.physd.2021.132927.
23. Kuznetsov NV, Leonov GA, Vagaitsev VI. Analytical-numerical method for attractor localization of generalized Chua's system. IFAC Proc. 2010;43(11):29–33. https://doi.org/10.3182/20100826-3-TR-4016.00009.
24. Leonov GA, Kuznetsov NV, Vagaitsev VI. Localization of hidden Chua's attractors. Phys Lett A. 2011;375(23):2230–3. https://doi.org/10.1016/j.physleta.2011.04.037.
25. Danca MF. Chaotic hidden attractor in a fractional order system modeling the interaction between dark matter and dark energy. Commun Nonlinear Sci Numer Simul. 2024;131:107838. https://doi.org/10.1016/j.cnsns.2024.107838.
26. Zhao PC,Wei HJ, Xu ZK, Chen DY, Xu BB,Wang YM. Existence of hidden attractors in nonlinear hydro-turbine governing systems and its stability analysis. Chinese Phys B. 2023;32(9):090503. https://doi.org/10.1088/1674-1056/acc8c4.
27. Obaid MJ, Neamah AA, Shukur A, Pham VT, Grassi G. A Reliable Color Image Encryption Scheme Based on a Novel Dual-Wing Hyperchaotic Map. Expert Syst Appl. 2025:128237. https://doi.org/10.1016/j.eswa.2025.128237.
28. Pisarchik AN, Hramov AE. Multistability in lasers. In: Multistability in Physical and Living Systems: Characterization and Applications. Springer International Publishing; 2022. p.167–98. https://doi.org/10.1007/978-3-030-98396-3_4.
29. Esqueda De La Torre JO, García López JH, Jaimes Reátegui R, Pisarchik AN, Huerta-Cuellar G. Effects of Optical Laser Injection in Multistable Erbium Fiber Lasers. Chaos Theor Appl. 2022;4(4):226–33. https://doi.org/10.51537/chaos.1197559.
30. Jabri H, Eleuch H. Optical bistability and multistability with coupled quantum wells in the presence of second-and third-order nonlinearities. Chaos Solit Fract. 2023;177:114270. https://doi.org/10.1016/j.chaos.2023.114270.
31. Li C, Sprott JC, Hu W, Xu Y. Infinite multistability in a self-reproducing chaotic system. Int J Bifurcat Chaos. 2017;27(10):1750160. https://doi.org/10.1142/S0218127417501607.
32. Zhao G, Zhao H, Zhang Y, An X. A new memristive system with extreme multistability and hidden chaotic attractors and with application to image encryption. Int J Bifurcat Chaos. 2024;34(01):2450010. https://doi.org/10.1142/S021812742450010X.
33. Wang X, Liu C, Zhao M, Yu H. A novel five-dimensional multistable hyperchaotic system with hidden attractors and its application in secure image transmission. Chaos Solit Fract. 2024;176:114053. https://doi.org/10.1016/j.chaos.2023.114053.
34. Pisarchik AN, Jaimes-Reátegui R, Rodríguez-Flores C, García-López J, Huerta-Cuéllar G, Martín-Pasquín FJ. Secure chaotic communication based on extreme multistability. J Franklin Institute. 2021;358(4):2561–75. https://doi.org/10.1016/j.jfranklin.2021.01.013.
35. Gokyildirim A, Kocamaz UE, Uyaroglu Y, Calgan H. A novel five-term 3D chaotic system with cubic nonlinearity and its microcontroller-based secure communication implementation. AEU-Int. J Electron Commu. 2023;160:154497. https://doi.org/10.1016/j.aeue.2022.154497.
36. Li C, Sprott JC, Akgul A, Iu HH, Zhao Y. A new chaotic oscillator with free control. Chaos. 2017;27(8). https://doi.org/10.1063/1.4997051.
37. Vijayakumar MD, Natiq H, Leutcho GD, Rajagopal K, Jafari S, Hussain I. Hidden and self-excited collective dynamics of a new multistablehyper-jerk system with unique equilibrium. Int J Bifurcat Chaos. 2022;32(5):2250063. https://doi.org/10.1142/S0218127422500638.
38. Vijayakumar MD, Jamal SS, Ali AM, Rajagopal K, Jafari S, Hussain I. Proposing and dynamical analysis of a hyperjerk piecewise linear chaotic system with offset boostable variable and hidden attractors. Complexity. 2021;2021(1):9037271. https://doi.org/10.1155/2021/9037271.
39. Pham VT, Vaidyanathan S, Volos CK, Jafari S, Wang X. A Chaotic Hyperjerk System Based on Memristive Device. In: Vaidyanathan S, Volos C, editors. Advances and Applications in Chaotic Systems. vol. 636 of Studies in Computational Intelligence. Cham: Springer; 2016. p. 15–34. https://doi.org/10.1007/978-3-319-30279-9_2.
40. Prousalis DA, Volos CK, Stouboulos IN, Kyprianidis IM. A 4D hyperjerk memristive system with hidden attractors. In: 2017 6th International Conference on Modern Circuits and Systems Technologies (MOCAST). IEEE;2017. p. 1–4. https://doi.org/10.1109/MOCAST.2017.7937652.
41. Zaamoune F, Tinedert IEH, Menacer T, Wang N. Multistability and Multi-Spiral Chaotic Sea in a Novel 3-D System with a Line of Equilibrium. Phys Scr. 2025;100(3):035226. https://doi.org/10.1088/1402-4896/adb3d8.
42. Ahmad I, Srisuchinwong B. On the First Single-Nonlinearity Seven-Term Memristor-Based Chaotic Snap System: A Line Equilibrium and Coexisting Hidden Attractors. In: 2019 24th International Conference on Methods and Models in Automation and Robotics (MMAR). IEEE;2019. p. 292–5. https://doi.org/10.1109/MMAR.2019.8864696.
43. Pham VT, Vaidyanathan S, Volos CK, Wang X, Hoang DV. A hyperjerk memristive system with hidden attractors. In: Advances in Memristors, Memristive Devices and Systems. vol. 701 of Studies in Computational Intelligence. Springer; 2017. p. 59–80. https://doi.org/10.1007/978-3-319-51724-7.
44. Shen M, Li C, Wang L, Xue Y, Qi X. More Diagonal Distributions of Coexisting Attractors. Symmetry. 2025;17(8):1331. https://doi.org/10.3390/sym17081331.
45. Zhang X, Chen M, Zhang R, Chen G. A note on the coexistence of infinitely many attractors. Chaos. 2025;35(5). https://doi.org/10.1063/5.0272999.
46. Li C, Shen M, Wang L, Xue Y, Qi X. Diagonal attractor self-reproducing via a single periodic function. Nonlinear Dyn. 2025;105:1–13. https://doi.org/10.1007/s11071-025-11681-4.
47. Mikaeel SH, Salih RH, Ahmad I. On the Dynamics of a Hyperjerk System and Its Reduction to the Generalized Michelson System. Int J Bifurcat Chaos. 2025;13:2550161. https://doi.org/10.1142/S0218127425501615.
48. Sambas A, Vaidyanathan S, Zhang S, Mohamed MA, Zeng Y, Azar AT. A new 4-D chaotic hyperjerk system with coexisting attractors, its active backstepping control, and circuit realization. In: Backstepping control of nonlinear dynamical systems. Elsevier; 2021. p. 73–94. https://doi.org/10.1016/B978-0-12-817582-8.00011-8.
49. Rajagopal K, Shekofteh Y, Nazarimehr F, Li C, Jafari S. A new chaotic multi-stable hyperjerk system with various types of attractors. Indian J Phys. 2022;96:1501–1507. https://doi.org/10.1007/s12648-021-02075-4.
50. Hahn W, others. Stability of Motion. Berlin: Springer; 1967. https://doi.org/10.1007/978-3-642-50085-5.
51. Singh JP, Roy BK. The simplest 4-D chaotic system with line of equilibria, chaotic 2-torus and 3-torus behaviour. Nonlinear

Dyn. 2017;89(3):1845–62. https://doi.org/10.1007/s11071-017-3556-4.
52. Shukur AA, Neamah AA, Pham VT, Grassi G. A novel chaotic system with one absolute term: stability, ultimate boundedness, and image encryption. Heliyon. 2025;11(1). https://doi.org/10.1016/j.heliyon.2024.e37239.
53. Wolf A, Swift JB, Swinney HL, Vastano JA. Determining Lyapunov exponents from a time series. Phys D Nonlinear Phenom. 1985;16(3):285–317. https://doi.org/10.1016/0167-2789(85)90011-9.
54. García-Martínez M, Ontañón-García L, Campos-Cantón E, Čelikovský S. Hyperchaotic encryption based on multi-scroll piecewise linear systems. Appl. Math. Comput. 2015;270:413–24. https://doi.org/10.1016/j.amc.2015.08.037.
55. Kamal F, Elsonbaty A, Elsaid A. A novel fractional nonautonomous chaotic circuit model and its application to image encryption. Chaos Solit Fract. 2021;144:110686. https://doi.org/10.1016/j.chaos.2021.110686.
56. Gan Zh, Chai Xl, Han Dj, Chen Yr. A chaotic image encryption algorithm based on 3-D bit-plane permutation. Neural Computing and Applications. 2019;31:7111–30. https://doi.org/10.1007/s00521-018-3541-y.
57. Wu Y, Noonan JP, Agaian S. NPCR and UACI randomness tests for image encryption. Journal of Selected Areas in Telecommunications. 2011;1(2):31–8.

عدد غير منتهي من الجذابات الخفية في نظام سناب فوضوي مكون من ستة عناصر ذو إطارين مع خط من نقاط الاتزان

سربست حسين ميكائيل[1]، عرفان احمد[2]، رزكار حاجي صالح[3]

[1]قسم الرياضيات، كلية العلوم، جامعة سوران، سوران، إقليم كردستان، العراق.
[2]كلية علوم الحاسوب والرياضيات، جامعة وايكاتو، نيوزيلندا.
[3]قسم الرياضيات، كلية التربية الأساسي، جامعة راپرين، إقليم كردستان، رانيه، العراق.

الخلاصة

النظم الفوضوية ذات البنى البسيطة والديناميكيات القابلة للتحكم مهمه جدا في التطبيقات العملية مثل الاتصالات الآمنة ومعالجة الإشارات، والتحكم غير الخطي. ومع ذلك، فإن معظم النظم الموجودة إما شديدة التعقيد أو تفتقر إلى المرونة في التحكم بسعة الإشارة وقطبيتها. في هذا العمل، نقترح نظام "سناب" فوضوي جديد وبسيط يتميز بخط من نقاط التوازن ويتكون من ستة حدود جبرية فقط، من بينها لاخطية والتي هي عباره عن دالة تربيعية. في بعض مناطق فضاء المعاملات يلتقي الجاذب الفوضوي مع خط توازن أو مع دورة حدية ذات فترة 2. ويكون حد الحوض بين الدورة الحدية والجاذب الفوضوي أملساً. بالإضافة إلى ذلك، في مناطق معينة، يمكن لدورتين حديثين أن تلتقيا معاً. وبهذا يصبح من الممكن الحصول على إشارة فوضوية بالسعة والقطبية المرغوبة على وجه الخصوص، يمكن تحويل نظام "سناب" الفوضوي المقترح إلى نظام ذاتي التوليد عن طريق إدخال دوال دورية دون التأثير على بنيته الأساسية. النظام الذاتي التوليد الناتج ينتج شبكة ثلاثية الأبعاد (3D) من الجاذبات الفوضوية والدورية الخفية، حيث يكون لعدد لانهائي من الجاذبات نفس مؤشرات ليابونوف. ونتيجة لذلك، يمكن الحصول على إشارة فوضوية بأي من القطبيتين عبر اختيار شروط ابتدائية مختلفة دون الحاجة إلى محول قطبية إضافي. تتيح هذه الخصائص تنفيذ دائرة رقمية تعتمد على العتاد من نوع STM32لإظهار الجدوى الفيزيائية للنظام المقترح. وأخيرًا، ولإثبات قابلية تطبيق نظام "سناب" المقترح في مجال تشفير الصور تم تصميم مولد أرقام عشوائية (RNG) وقد نجح المولد الناتج في اجتياز الاختبارات الإحصائية NIST SP 800-22الصادرة عن المعهد الوطني للمعايير والتقنية (NIST) ، مما يؤكد قدرته العالية على توليد العشوائية. وبناء على هذه البتات العشوائية، تم تطوير خوارزمية لتشفير الصور. وتظهر تحليلات الأمان أن النظام المقترح قادر على تشفير وفك تشفير الصور بفعالية مع تحقيق أداء أمني مرتفع.

الكلمات المفتاحية: السعة والقطبية، التنفيذ العتادي، الجاذبات المخفية، تشفير الصور، التعددية في الاستقرار، النظام ذاتي الاستنساخ، نظام السناب.